Probing the Active Surface Sites for CO Reduction on Oxide-Derived Copper Electrocatalysts

A. Verdaguer-Casadevall, C. W. Li, T. P. Johansson, S. B. Scott, J. T. McKeown, I. E. Stephens, M. Kumar, M. W. Kanan, I. Chorkendorff

June 11, 2015

Disclaimer

This document was prepared as an account of work sponsored by an agency of the United States government. Neither the United States government nor Lawrence Livermore National Security, LLC, nor any of their employees makes any warranty, expressed or implied, or assumes any legal liability or responsibility for the accuracy, completeness, or usefulness of any information, apparatus, product, or process disclosed, or represents that its use would not infringe privately owned rights. Reference herein to any specific commercial product, process, or service by trade name, trademark, manufacturer, or otherwise does not necessarily constitute or imply its endorsement, recommendation, or favoring by the United States government or Lawrence Livermore National Security, LLC. The views and opinions of authors expressed herein do not necessarily state or reflect those of the United States government or Lawrence Livermore National Security, LLC, and shall not be used for advertising or product endorsement purposes.

Probing the active surface sites for CO reduction on oxide-derived copper electrocatalysts

Arnau Verdaguer-Casadevall,[1‡] Christina W. Li,[2‡] Tobias P. Johansson,[1] Soren B. Scott,[1] Joseph T. McKeown,[3] Ifan E. L. Stephens,[1] Mukul Kumar,[4] Matthew W. Kanan,[2*] and Ib Chorkendorff[1*]

[1] Center for Individual Nanoparticle Functionality, Department of Physics, Building 312, Technical University of Denmark (DTU), DK-2800, Kongens Lyngby, Denmark
[2] Department of Chemistry, Stanford University, 337 Campus Drive, Stanford, CA 94305, United States
[3] Materials Science Division, Lawrence Livermore National Laboratory, 7000 East Avenue, Livermore, CA 94550, United States
[4] Materials Engineering Division, Lawrence Livermore National Laboratory, 7000 East Avenue, Livermore, CA 94550, United States

ABSTRACT: CO electroreduction activity on oxide-derived Cu (OD-Cu) was found to correlate with metastable surface features that bind CO strongly. Temperature programmed desorption of CO on OD-Cu reveals the presence of surface sites with strong CO binding that are distinct from the terraces and stepped sites found on polycrystalline Cu foil. As prepared, OD-Cu reduces CO to acetate and ethanol with nearly 50 % Faradaic efficiency at moderate overpotential. Thermal annealing attenuates electrocatalytic activity; after annealing at 350 °C, the specific current density for CO reduction is reduced 44-fold and the Faradaic efficiency for ethanol and acetate is less than 5%. The loss of activity is correlated with a reduction in both the proportion of strong CO binding sites and in the bulk grain boundary density as assessed by orientation mapping using electron nanodiffraction. We propose that metastable grain boundary surface sites with strong CO binding are responsible for the high CO reduction activity and selectivity of OD-Cu catalysts. Identification of these sites is a first step towards understanding the surface chemistry necessary for efficient CO electroreduction.

The use of renewable energy to convert CO_2 into chemicals and fuels is an attractive means of mitigating emissions and increasing energy security.[1,2] Electrochemical CO_2 conversion could be pivotal to this goal; electrolyzers allow for fast startup and require little infrastructure, which would enable deployment of decentralized CO_2 recycling units scaled to local renewable energy sources.[3]
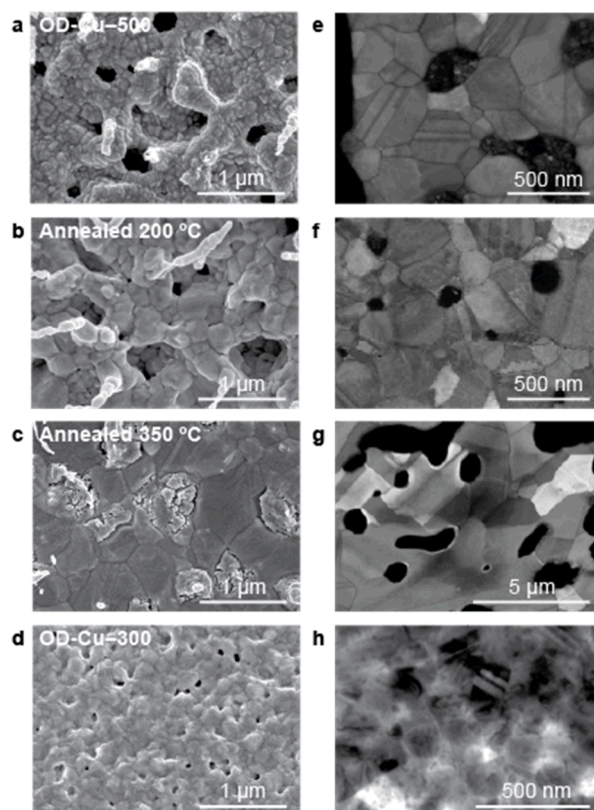

Figure 1. (a-d) SEM images, (e-g) image quality (IQ) maps constructed from electron diffraction data, and (h) TEM image of oxide-derived Cu electrodes. (a, e) OD-Cu oxidized at 500 °C and reduced in H_2 (OD-Cu–500), (b, f) OD-Cu–500 after 200 °C anneal in inert atmosphere, (c, g) after 350 °C anneal in inert atmosphere, (d, h) OD-Cu oxidized at 300 °C and reduced in H_2 (OD-Cu–300).

One strategy for efficient electrochemical CO_2 conversion is to separate the process into two steps: CO_2 reduction to CO, followed by CO reduction to oxygenates and hydrocarbons. Moreover, several promising CO_2 reduction catalysts have recently been reported that may enable practical CO_2 to CO conversion at low temperature.[4-14] While Cu is the only metal with appreciable activity for CO reduction, the separation of this process from CO_2 reduction enables it to be performed in alkaline solution, where the selectivity for C2 products is enhanced.[15,16] The key challenge is to increase the activity of Cu at low overpotential. We recently showed that nanocrystalline Cu prepared via reduction of a Cu_2O precursor, "oxide-derived Cu" (OD-Cu), has unprecedented activity for the reduction of CO to oxygenates.[17] At potentials as positive as -0.25 V vs the reversible hydrogen electrode (RHE), OD-Cu reduces CO with >50 % Faradaic efficiency; for ethanol this equates to an overpotential of 0.43 V; for acetate this equates to an overpotential of 0.75 V. Thus far, the origin of CO reduction activity on OD-Cu, particularly the identity of the catalytically active surface site, remains elusive. Based on TEM studies, we proposed that the catalytic activity for CO reduction was associated with the presence of grain boundaries.[17,18] However, catalysis is a surface phenomenon, whereas grain boundaries are bulk defects. More detailed understanding of the active surfaces of OD-Cu will enable the development of catalysts with even greater improvements in selectivity and activity.

This study examines the importance of microstructure on the thermodynamics of adsorbate binding at the surface and how those thermodynamics in turn impact catalytic activity. Thermal annealing of OD-Cu in inert atmosphere demonstrates that both the nanograined structure and CO reduction activity of OD-Cu are metastable. Temperature-programmed desorption (TPD) of CO is then used to probe the surface chemistry of OD-Cu and its thermally deactivated derivatives. CO-TPD provides information on the strength of CO binding to surface sites, which has obvious implications for electrocatalytic CO

reduction.[19] Previous CO-TPD studies on single-crystalline Cu surfaces have shown that desorption peak position is diagnostic of the surface facet involved in CO binding. TPD has been widely used to study heterogeneous catalysts such as $Cu/ZnO/Al_2O_3$ for methanol synthesis[19,20] but thus far has seldom been used to study electrocatalytic surfaces.[21-23]

OD-Cu samples are synthesized via air oxidation at 500 °C followed by H_2 reduction at 130 °C (herein referred to as OD-Cu–500).[17] Scanning and transmission electron microscopy indicate irregularly shaped grains that are 100-300 nm in size, aggregated into a dense polycrystalline network (Fig. 1a, e). In order to modulate the catalytic activity and grain size of OD-Cu, a reduced OD-Cu electrode is subsequently annealed under vacuum or inert atmosphere at 200 °C and 350 °C. Thermal post-annealing results in an increase of the average grain size to ~500 nm and ~1 um at 200 °C and 350 °C, respectively (Fig. 1b, c, f, g). Nonetheless, the dense polycrystalline network observed in OD-Cu, consisting of crystallites bounded by grain boundaries, is still present in the thermally annealed samples. For comparison, an oxide-derived Cu electrode, oxidized in air at 300 °C for 30 min. and reduced in H_2 at 130 °C (OD-Cu–300), was also prepared. It exhibited a relatively smooth morphology with grain sizes in the 200 nm range (Fig 1d, h).

X-ray diffraction and X-ray photoelectron spectroscopy (XPS) of all four samples indicate that the only bulk crystalline phase present is Cu^0, and the surface comprises primarily Cu^0 with some Cu^{1+} due to native oxide formation during transfer of the sample to the XPS chamber (Fig SX). The electrochemically active surface area of each sample was assessed using an electrochemical capacitance measurement. OD-Cu–500 has a roughness factor of 51 (where polycrystalline Cu is 1), arising from the high surface area porous structure. As anticipated from the grain growth observed in the SEM and TEM, the roughness factor of the electrode drops from 51 to 24 and 14 as oxide-derived Cu is annealed at 200 °C and 350 °C, respectively. This is a consequence of both grain growth and flattening of the elec-

trode during the annealing process. OD-Cu–300 has a roughness factor of 6, lower than that of both thermally annealed electrodes.

Electrochemical activity for CO reduction was assessed over a range of potentials via constant potential electrolysis in 0.1 M KOH electrolyte, continuously purged with 1 atm of CO. The CO reduction activity of OD-Cu–500 has been previously reported. OD-Cu–500 exhibits peak Faradaic efficiency of 48% for CO reduction at –0.4 V vs. RHE and generates C2 and C3 products including acetate, ethanol, propanol, ethylene, and ethane (Fig 2a), measured by gas chromatography and nuclear magnetic resonance (NMR). The surface-area normalized partial current density for CO reduction increases with increasing overpotential but rapidly reaches a plateau corresponding to the mass-transport limit of ~1 mM dissolved CO in water (Fig 2c). [24]

Upon annealing, the intrinsic CO reduction activity of the electrode is significantly reduced. The surface-area corrected partial current density for CO reduction (j_{CORedn}) is attenuated 6-fold on the 200 °C-annealed sample and 44-fold on the 350 °C-annealed sample, relative to as-prepared OD-Cu–500 (Fig. 2c). This suggests that

the catalytically active sites are tied to metastable microstructural features such as defects and grain boundaries, which are kinetically trapped during the low-temperature H_2 reduction process.

The catalytic activity of OD-Cu can also be modified by altering the properties of the precursor oxide. OD-Cu–300 is produced from a thinner oxide precursor and is intrinsically less active for CO reduction than OD-Cu–500. In fact, it has very similar specific j_{CORedn} to the partially deactivated, 200 °C-annealed sample, despite a significantly lower roughness factor. The partial current densities for CO reduction at –0.3 V vs. RHE for OD-Cu–300 and the 350 °C-annealed electrode were too low for reliable NMR detection. The normalized partial current density for H_2 (j_{H2}) evolution remains essentially unchanged regardless of thermal annealing or oxidation temperature (Fig 2d).

The loss of intrinsic CO reduction activity upon thermal annealing is reflected in the Faradaic efficiencies for CO reduction at –0.4 V vs. RHE (Fig 2a). The relative ratios of oxygenate to hydrocarbon products remain similar, but there is a drop in total Faradaic efficiency for CO reduction and a corresponding increase in Faradaic efficiency for H_2 evolution. While the 200 °C-annealed sample still shows modest activity for CO reduction, attaining 30% total Faradaic efficiency, the 350 °C-annealed sample is essentially unselective for CO reduction. OD-Cu–300 reaches 31% total Faradaic efficiency, again very similar to the 200 °C-annealed electrode. The fact that two electrodes with very different roughness factors have identical specific activities and Faradaic efficiencies for CO reduction indicates that electrode porosity or microscopic surface area is not a significant determinant of CO reduction catalytic activity.

We previously hypothesized that the active sites for CO reduction are located at the disordered surfaces associated with grain boundary terminations.[17] To quantify the grain-boundary character distributions, orientation maps were collected from the OD-Cu-500 and the 350 °C
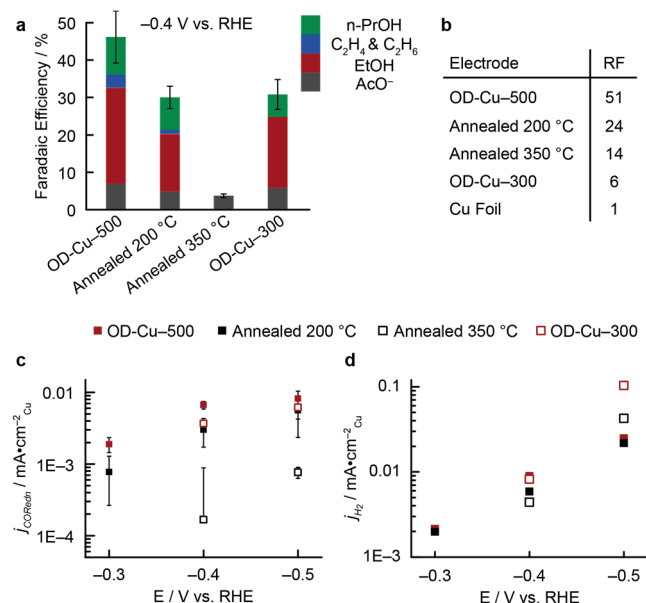

Figure 2. (a) Faradaic efficiency for CO reduction at –0.4 V vs. RHE in CO-saturated 0.1 M KOH. The remainder of the charge passed is in production of H_2. (b) electrochemical roughness factors (RF), measured from the capacitance in a non-Faradaic potential regime, with Cu foil defined as 1. (c) Specific current density for CO reduction vs. potential. (d) Specific current density for H_2 evolution vs. potential. The error bars represent one standard deviation from the mean based on 2-5 independent measurements.

Electrode	RF
OD-Cu–500	51
Annealed 200 °C	24
Annealed 350 °C	14
OD-Cu–300	6
Cu Foil	1

thermally deactivated samples. This TEM-based technique collects nanodiffraction patterns from scanned regions of the samples, providing information for nanostructures analogous to that acquired using EBSD mapping in an SEM. These data are subsequently indexed to generate grain orientation and grain boundary maps from which grain boundary density and misorientation angles can be extracted (Figure SX). While this technique provides information on bulk grain boundary densities rather than surface densities, the bulk and surface values can be correlated by constant factors derived from the shape and size of the grains. From this analysis, OD-Cu–500 has an average grain boundary density of 14 ± 2 μm^{-1}. Upon annealing at 350 °C, the overall grain boundary density drops to 2.1 ± 0.4 μm^{-1}, commensurate with grain growth observed during thermal treatment (Fig SX). In addition, the fraction of low-energy twin boundaries relative to randomly oriented boundaries increases during the annealing process. The effects of thermal annealing on both microstructure and catalytic activity provide evidence for the importance of grain boundary surface sites in catalysis. Thermal annealing reduces the grain boundary density via grain growth and reduces j_{CORedn} while leaving j_{H2} unaffected. This result suggests that the CO reduction activity may be funneled through a relatively small number of highly active sites that are associated with grain boundaries while the remainder of the surface behaves essentially like polycrystalline Cu foil. In order to connect the microstructural and catalytic changes to the thermodynamics of adsorbate binding on the surface, CO-TPD was used to further probe the surface chemistry of OD-Cu.

The OD-Cu samples for TPD were oxidized ex-situ and mounted in the UHV chamber. Adventitious contamination from exposure to air was removed by mildly sputtering the surface, and the samples were subsequently reduced at 130 ºC under a flow of 1 bar of H$_2$ (see the Supporting Information). XPS at this stage showed a metallic Cu surface (Fig. S12) with no trace of nickel (a common contaminant in UHV in the presence of CO due to the formation of nickel carbonyl in
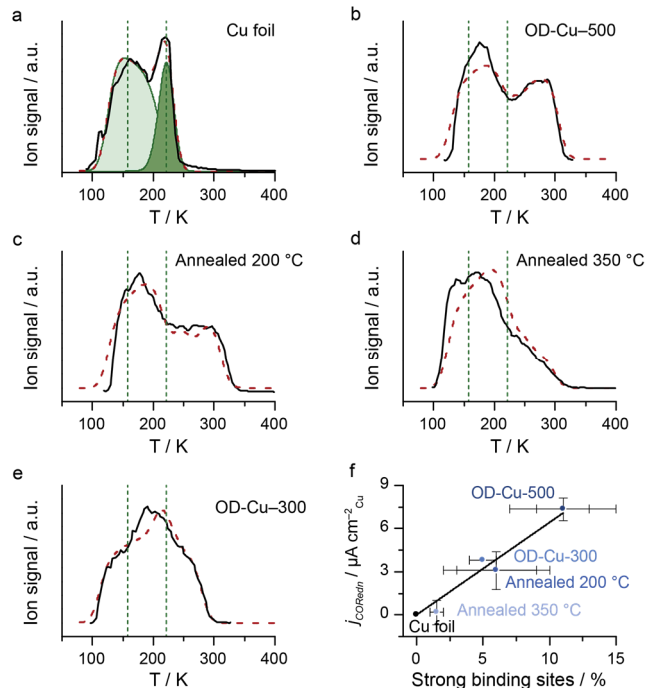
Figure 3. TPD profiles for various Cu samples. a-e) Experimental data (solid black lines) and resulting fit from microkinetic simulations (dashed red lines). The dotted green lines indicate the central position of the low-index facets and stepped sites in polycrystalline Cu. a) Polycrystalline Cu. Features arising from low-index facets are highlighted in light green, undercoordinated sites are highlighted in dark green; b) OD-Cu–500; c) OD-Cu annealed at 200 °C; d) OD-Cu annealed at 350 °C; e) OD-Cu–300; f) overlay of TPD profiles. Measurements were performed at a ramp rate of 2 K s^{-1} with a CO dose of 200 L. g) Experimental CO reduction activity at –0.4 V as a function of the percentage of strong binding sites, estimated from simulations of the TPD profiles. The solid black line is a linear fit through all points. The error bars are a means of showing uncertainty in the simulations and have been obtained by varying pore depth in the model by ±5 μm or 50 %, whichever is lowest.

the gas lines[25]) or other metallic impurities. The samples were cooled down to 77 K, and CO was dosed into the chamber. The temperature was then ramped up at 2 K s^{-1} and a mass spectrometer monitored the signal from CO at mass 28. The annealed OD-Cu samples were prepared in an identical manner to OD-Cu–500 and annealed in UHV at 200 °C or 350 °C prior to CO dosing. The experiments were carried out with a constant dosage of 200 L, which results in variable CO coverage (Fig. S10). given the different surfaces areas of the samples.

Figure 3a shows a typical TPD profile for electropolished polycrystalline Cu foil. Based on literature data from single crystalline Cu,[19,26,27] the TPD features can be assigned to different facet terminations. The lowest temperature desorption feature, from 100 K to 200 K is due to low index facets such as Cu(111) and Cu(100), which

bind CO weakly. The higher temperature feature between 200 K and 250 K is representative of stepped sites such as Cu(211). Figure 3b shows the CO-TPD profile on OD-Cu–500. The OD-Cu–500 profile shows a high-temperature feature centered at 275 K that is clearly absent from the profiles for polycrystalline Cu and single crystalline Cu but is present in different proportions in the profiles for the other OD-Cu samples (Fig. 3f). Annealing OD-Cu–500 to 200 °C and 350 °C reduces the area of the high-temperature feature (Figures 3c-d). The profile of OD-Cu–300 exhibits broader and less-defined peaks than OD-Cu–500 and its annealed derivatives due to the higher coverage of CO on the low roughness factor electrode, but the high-temperature feature is clearly still present (Fig. 3e-f).

Two possible factors could account for the high-temperature feature in the OD-Cu profiles: (i) CO readsorption in the catalyst layer, which causes peak broadening and a shift of the peak maximum to higher temperature or (ii) surface sites with enhanced binding to CO. Both of these effects have been observed in TPD studies on industrial Cu/ZnO/Al$_2$O$_3$ and Cu/SiO$_2$ catalysts.[28,29] Readsorption likely plays a role in the high-temperature feature on OD-Cu materials. OD-Cu–500 has a large roughness factor, and a significant fraction of the sample surface may reside in mesopores where readsorption could easily occur. However, OD-Cu–300 has a roughness factor of only 6, which is the lowest of the OD-Cu samples and 2.5-fold lower than the 350 °C-annealed sample. Despite its lower roughness factor, OD-Cu–300 presents a higher proportion of the high-temperature feature than the 350 °C annealed sample, indicating that readsorption alone cannot account for the high-temperature feature on OD-Cu.

To determine the contribution of readsorption to the OD-Cu profile, we carried out TPD simulations of porous polycrystalline Cu, assuming the presence of two binding sites with adsorption energies of about 52 and 60 kJ/mol, corresponding to low-index and stepped facets of Cu (described in the Supporting Information). As shown in Figure S16, increasing the depth of the porous layer causes a shift of the polycrystalline Cu foil TPD profile to higher temperature. While simulated porous polycrystalline Cu has a major peak at 260 K, the overall profile clearly does not fit that of OD-Cu. We could only model the experimental TPD profile for the OD-Cu samples by including a strong binding site with adsorption energy of 67 kJ/mol.

Direct quantitative interpretation of the TPD profiles shown here is not possible because the roughness factor of each sample is different. The same CO dosage gives variations in surface coverage and differing degrees of readsorption on each sample, both of which affect the relative proportions of the low-index, stepped, and strong-binding TPD features. In particular, CO binds preferentially to the strongest binding site; consequently, the proportion of the high-temperature feature will exceed the surface fraction of the strong binding site at low initial coverage. Microkinetic models of CO binding to each OD-Cu surface (Fig. 3a-e) enable the decoupling of these effects and provide an estimate of the relative abundance of strong binding sites. Based on these simulations, OD-Cu–500 has the largest proportion of strong-binding sites with 11% surface coverage. The proportion drops to 5% after annealing at 200 °C and 1.5% after annealing at 350 °C. While these percentages have large uncertainty due to assumptions made about the electrode pore structure, the proportion of strong-binding sites is clearly reduced through thermal annealing. When plotted against electrochemical activity, a linear correlation is obtained between specific CO reduction rate and the percentage of strong binding sites at the electrode surface (Fig 3f), suggesting that these sites are involved in the electrocatalytic reaction with CO.

We hypothesize that low overpotential CO reduction occurs at the surface sites with strong CO binding. A high density of sites with stronger binding to CO may increase the equilibrium coverage of CO at the surface and lower the activation barrier for C-C coupling[30,31], thus enhancing the overall rate for CO reduction. However, these active sites may be necessary but not suf-

ficient for CO reduction. The completely deactivated form of OD-Cu (350 °C-annealed) retains 1.5% of the strong binding site despite having j_{CORedn} lower than that of polycrystalline Cu foil, which has only terrace and step sites (Table S3). The broad high-temperature feature observed in TPD does not reflect a single surface atomic structure; rather it most likely consists of a range of strained or defective structures, all of which bind CO more strongly within a ~10 kJ/mol range. As such, it is possible that only a small subset of those defective structures are capable of catalyzing the CO reduction reaction. In addition, CO is simply a probe molecule in these experiments. In electrolyte solution with an applied potential, the relevant catalytic transition state structures and binding energies may not scale with the CO binding energy in UHV.

The reduction in the proportion of strong binding sites upon thermal annealing qualitatively correlates to the microstructural change observed in TEM. The 7-fold drop in strong binding percentage is similar to the 7-fold drop in grain boundary density observed between OD-Cu-500 and the electrode after 350 °C annealing. Based on these data, we hypothesize that the strong-binding site is present at defect or grain boundary surface terminations, which are uniquely active for CO reduction electrocatalysis. Previous studies have shown that grain boundary surface terminations in fcc metals can exhibit significantly altered structures relative to the common low-index and stepped facets.[32] Grain boundary density has also been correlated to CO_2 and CO reduction catalytic activity on vapor-deposited nanocrystalline Au and Cu supported on carbon nanotubes. [cite XF]

Due to uncertainty in the pore structure of the high surface area OD-Cu materials, there are large error bars in the calculation of surface site abundance from the TPD data. However, even the rough estimation of 7-15% strong binding site on OD-Cu-500 indicate that a much larger proportion of the surface is structurally and energetically perturbed than the TEM images initially indicate. Based on the nanodiffraction grain boundary maps and assuming a 1 nm boundary width, we estimate that OD-Cu-500 has 1-2% coverage of grain boundary surface area while the 350 °C-annealed electrode has ~0.2 % coverage. The TPD data suggests that the surfaces in the vicinity of grain boundaries, encompassing a much larger width of 4-10 nm, may also be significantly strained. Alternatively, the oxide-reduction process may generate other defects such as dislocations that are not readily observed in the TEM nanodiffraction scans.

In summary, we present evidence that the high CO reduction activity on OD-Cu is correlated to surface sites that bind CO more strongly than low-index and stepped Cu facets. These metastable sites may arise from the disordered surfaces at grain boundary and defect terminations, which are stabilized by the interconnected nanocrystalline network. Further structural and mechanistic elucidation of the surface chemistry of OD-Cu, in particular regarding the exact nature of the active site, will enable the design and synthesis of more efficient catalytic materials for CO reduction.

ASSOCIATED CONTENT

Supporting Information

Experimental procedures and additional data. This material is available free of charge via the Internet at http://pubs.acs.org.

AUTHOR INFORMATION

Corresponding Authors

*mkanan@stanford.edu, ibchork@fysik.dtu.dk

Author Contributions

‡These authors contributed equally to this work.

Notes

The authors declare no competing financial interests.

REFERENCES

(1)   Hori, Y. In *Modern Aspects of Electrochemistry*; Vayenas, C., White, R., Gamboa-Aldeco, M., Eds.; Springer New York: 2008; Vol. 42, p 89.

(2)   Appel, A. M.; Bercaw, J. E.; Bocarsly, A. B.; Dobbek, H.; DuBois, D. L.; Dupuis, M.; Ferry, J. G.; Fujita, E.; Hille, R.; Kenis, P. J. A.; Kerfeld, C. A.; Morris, R. H.; Peden, C. H. F.; Portis, A. R.; Ragsdale, S. W.; Rauchfuss, T. B.; Reek, J. N. H.; Seefeldt, L. C.; Thauer, R. K.; Waldrop, G. L. *Chem Rev* **2013**, *113*, 6621.

(3)   Gasteiger, H. A.; Garche, J. In *Handbook of Heterogeneous Catalysis*; Wiley-VCH: Weinheim, 2008, p 3081.

(4)   Rosen, B. A.; Salehi-Khojin, A.; Thorson, M. R.; Zhu, W.; Whipple, D. T.; Kenis, P. J. A.; Masel, R. I. *Science* **2011**, *334*, 643.

(5)   Chen, Y. H.; Li, C. W.; Kanan, M. W. *J Am Chem Soc* **2012**, *134*, 19969.

(6)   DiMeglio, J. L.; Rosenthal, J. *J Am Chem Soc* **2013**, *135*, 8798.

(7)   Zhu, W. L.; Michalsky, R.; Metin, O.; Lv, H. F.; Guo, S. J.; Wright, C. J.; Sun, X. L.; Peterson, A. A.; Sun, S. H. *J Am Chem Soc* **2013**, *135*, 16833.

(8)   Manthiram, K.; Surendranath, Y.; Alivisatos, A. P. *J Am Chem Soc* **2014**, *136*, 7237.

(9)   Kuhl, K. P.; Hatsukade, T.; Cave, E. R.; Abram, D. N.; Kibsgaard, J.; Jaramillo, T. F. *J Am Chem Soc* **2014**, *136*, 14107.

(10)   Mistry, H.; Reske, R.; Zeng, Z. H.; Zhao, Z. J.; Greeley, J.; Strasser, P.; Cuenya, B. R. *J Am Chem Soc* **2014**, *136*, 16473.

(11)   Lu, Q.; Rosen, J.; Zhou, Y.; Hutchings, G. S.; Kimmel, Y. C.; Chen, J. G. G.; Jiao, F. *Nat Commun* **2014**, *5*.

(12)   Porosoff, M. D.; Yang, X. F.; Boscoboinik, J. A.; Chen, J. G. G. *Angew Chem Int Edit* **2014**, *53*, 6705.

(13)   Asadi, M.; Kumar, B.; Behranginia, A.; Rosen, B. A.; Baskin, A.; Repnin, N.; Pisasale, D.; Phillips, P.; Zhu, W.; Haasch, R.; Klie, R. F.; Kral, P.; Abiade, J.; Salehi-Khojin, A. *Nat Commun* **2014**, *5*, 4470.

(14)   Rasul, S.; Anjum, D. H.; Jedidi, A.; Minenkov, Y.; Cavallo, L.; Takanabe, K. A. *Angew Chem Int Edit* **2015**, *127*, 2174.

(15)   Hori, Y.; Takahashi, R.; Yoshinami, Y.; Murata, A. *J Phys Chem B* **1997**, *101*, 7075.

(16)   Schouten, K. J. P.; Qin, Z. S.; Gallent, E. P.; Koper, M. T. M. *J Am Chem Soc* **2012**, *134*, 9864.

(17)   Li, C. W.; Ciston, J.; Kanan, M. W. *Nature* **2014**, *508*, 504.

(18)   Li, C. W.; Kanan, M. W. *J Am Chem Soc* **2012**, *134*, 7231.

(19)   Fu, S. S.; Somorjai, G. A. *Surf Sci* **1992**, *262*, 68.

(20)   Sandoval, M. J.; Bell, A. T. *Journal of Catalysis* **1993**, *144*, 227.

(21)   Perez-Alonso, F. J.; McCarthy, D. N.; Nierhoff, A.; Hernandez-Fernandez, P.; Strebel, C.; Stephens, I. E. L.; Nielsen, J. H.; Chorkendorff, I. *Angew Chem Int Edit* **2012**, *51*, 4641.

(22)   van der Niet, M. J. T. C.; den Dunnen, A.; Juurlink, L. B. F.; Koper, M. T. M. *Angew Chem Int Edit* **2010**, *49*, 6572.

(23)   Johansson, T. P.; Ulrikkeholm, E. T.; Hernandez-Fernandez, P.; Escudero-Escribano, M.; Malacrida, P.; Stephens, I. E. L.; Chorkendorff, I. *Physical Chemistry Chemical Physics* **2014**, *16*, 13718.

(24)   In *IUPAC Solubility Data Series*; Cargill, R. W., Ed.; Pergamon Press: Oxford, 1990; Vol. 43.

(25)   Nerlov, J.; Sckerl, S.; Wambach, J.; Chorkendorff, I. *Applied Catalysis A: General* **2000**, *191*, 97.

(26)   Vollmer, S.; Witte, G.; Woll, C. *Catal Lett* **2001**, *77*, 97.

(27)   Makino, T.; Okada, M. *Surf Sci* **2014**, *628*, 36.

(28)   Strunk, J.; d'Alnoncourt, R. N.; Bergmann, M.; Litvinov, S.; Xia, X.; Hinrichsen, O.; Muhler, M. *Phys Chem Chem Phys* **2006**, *8*, 1556.

(29)   d'Alnoncourt, R. N.; Bergmann, M.; Strunk, J.; Loffler, E.; Hinrichsen, O.; Muhler, M. *Thermochim Acta* **2005**, *434*, 132.

(30)   Calle-Vallejo, F.; Koper, M. T. M. *Angewandte Chemie International Edition* **2013**, *52*, 7282.

(31)   Montoya, J. H.; Peterson, A. A.; Nørskov, J. K. *ChemCatChem* **2013**, *5*, 737.

(32)   Lancon, F.; Radetic, T.; Dahmen, U. *Phys Rev B* **2004**, *69*.

(33)   Gunter, M. M.; Ressler, T.; Bems, B.; Buscher, C.; Genger, T.; Hinrichsen, O.; Muhler, M.; Schlogl, R. *Catal Lett* **2001**, *71*, 37.

(34)   Behrens, M.; Studt, F.; Kasatkin, I.; Kühl, S.; Hävecker, M.; Abild-Pedersen, F.; Zander, S.; Girgsdies, F.; Kurr, P.; Kniep, B.-L.; Tovar, M.; Fischer, R. W.; Nørskov, J. K.; Schlögl, R. *Science* **2012**, *336*, 893.